

# Understanding and Modeling the Resistance of High Aspect Ratio FIB-Fabricated Tungsten Vias

David W. Niles, Walter Dauksher, and Ronald W. Kee

(Submitted September 17, 2009)

Tungsten vias, made with traditional focused ion beam (FIB) techniques for the purpose of circuit edit work, exhibit higher electrical resistance than expected from the resistivity of the deposited tungsten and the via's geometry. The resistance is a strong function of the via's aspect ratio, defined here, to be the length of the via divided by its area. Chemical analysis of the vias shows that a poorly conductive skin of partially reacted  $W(CO)_6$  precursor and thickness  $\sim 0.1 \mu\text{m}$  lines the perimeter of every via. The skin is an unwanted consequence of the traditional technique used for filling a via with tungsten to prohibit the formation of voids. The existence of a poorly conductive perimeter justifies an effective area model whereby the electrical area of the via is the drawn area minus the area of the poorly conductive perimeter. The effective area model lends itself to two theoretical frameworks: one employing closed-form analytical expressions, and the second using finite element analysis, for understanding electrical resistance as a function of aspect ratio. The finite element framework adheres strictly to the known geometry of the vias, accounts for current crowding, and presents a reasonable fit to the data.

**Keywords** advanced characterization, electronic materials, micro-electronic failure analysis

## 1. Introduction

Classical electromagnetic theory mandates that the resistance of a tungsten via drawn in a focused ion beam (FIB) for the purpose of editing circuit functionality should follow the law

$$R = \rho L/A, \quad (\text{Eq } 1)$$

where  $\rho$  is the resistivity of the tungsten,  $L$  is the length of the via, and  $A$  is the area of the via (Ref 1). A common definition for the aspect ratio of a via is the length divided by the width, a dimensionless quantity suitable for square or circular vias (Ref 2). For rectangular vias, the most commonly employed by the FIB community, an alternative definition for the aspect ratio is

$$\text{Aspect Ratio} = L/A,$$

which, though having the disadvantage of an inverse length dimension, is amenable to placing various shaped vias (e.g., rectangles, circles, etc.) on a similar footing and is consistent with Eq 1. This latter definition of the aspect ratio is employed in this article.

Figure 1 shows the resistances of square vias plotted against their aspect ratios. This figure was first published in Ref 3 along with the conclusion that simple electromagnetic theory failed for FIB-made vias (Ref 3). The resistance from Eq 1 ought to be linear with aspect ratio but deviates to higher values with

increasing aspect ratio. The data in Fig. 1 fit to either of the two experimental models: (1) an effective area model that mandated a non-conductive skin around the perimeter of the via, and (2) an interface contact resistance model that mandated a poorly conductive barrier between the via and the bottom metal layer. Both fits are shown in Fig. 1. At the time of publication of Ref 3, the effective area and contact resistance models were relegated to little more than ruses because experimental guidance to understand and to develop the physics behind them was not extant. They simply worked.

In addition to solid physical bases, acceptable models for the resistances of the vias also need to account for current crowding (Ref 4). Current crowding concepts should be more prevalent in small aspect ratio vias where Eq 1 seems to work fairly well. The idea is that the charge carriers crowd to the edges of the vias when they enter the bottom sheet metal layer, thereby decreasing the effective area near the via bottom.

The purpose of this study is to develop a physical and materials-based model to explain the observed deviation of resistance from linearity with respect to aspect ratio, and to develop a theoretical framework for fitting the resistance data. Of the two models presented in Ref 3, the contact resistance model fails and contradicts a logical description of FIB via fabrication methodology. The effective area model works. FIB via fabrication methodology leaves a skin of partially reacted  $W(CO)_6$  along the walls of the via, which electrically behaves as a poorly conductive perimeter. The expected thickness of the poorly conductive sidewall is consistent with the value needed to fit the experimental data. These results kill the contact resistance model while exculpating the effective area model from its stature as a ruse.

## 2. Experimental

The experimental conditions used for the data in Fig. 1 are described in Ref 3. The experimental conditions for the data

David W. Niles, Walter Dauksher, and Ronald W. Kee, Avago Technologies, Fort Collins, CO. Contact e-mail: david.niles@avago.tech.com.

collected during these experiments were similar. Test wafers were 2.5  $\mu\text{m}$  of  $\text{SiO}_2$  made from tetra-ethyl-ortho-silicate (TEOS), deposited on a 2.5- $\mu\text{m}$  layer of evaporated Al on a Si substrate.

Standard FIB techniques were used on a Vectra Vision FIB to manufacture vias in the  $\text{SiO}_2$  films (Ref 2, 3, 5). Figure 2 shows the geometry of the via structures. A 50  $\mu\text{m} \times 50 \mu\text{m}$  hole in the  $\text{SiO}_2$  served as an access point for one electrode. The high aspect ratio vias (typically 0.3  $\mu\text{m} \times 0.3 \mu\text{m}$ ) were milled in the  $\text{SiO}_2$  and coated with a 0.54- $\mu\text{m}$ -thick W pad on top to serve as the second electrode. The milling conditions for the vias were a 23 pA beam, a pixel spacing of 0.01  $\mu\text{m}$  in both  $x$  and  $y$ , and a dwell time of 5  $\mu\text{s}$ , and  $\text{XeF}_2$  etch assistance at a reservoir pressure of 1.3 Torr. Standard techniques for filling a via with W were used. For instance, in order to fill a 0.3  $\mu\text{m} \times 0.3 \mu\text{m}$  via with tungsten, the  $\text{Ga}^+$  beam rasters over the center of the via hole, leaving a 0.1- $\mu\text{m}$  border around the perimeter to prevent pinch-off and void formation (Ref 2). For a 0.3  $\mu\text{m} \times 0.3 \mu\text{m}$  via, the filling raster would be 0.1  $\mu\text{m} \times 0.1 \mu\text{m}$ .

Varying the length of a via involved pre-milling a 5  $\mu\text{m} \times 5 \mu\text{m}$  hole in the  $\text{SiO}_2$  layer to the desired depth and then making a via in the center of this hole with the aforementioned

conditions. The milling parameters for the 5  $\mu\text{m} \times 5 \mu\text{m}$  holes were a 930 pA beam, a pixel spacing of 0.05  $\mu\text{m}$  in both  $x$  and  $y$ , a dwell time of 1  $\mu\text{s}$ , and  $\text{XeF}_2$  etch assistance at a nozzle pressure of 1.3 Torr. The milling rate for the 5  $\mu\text{m} \times 5 \mu\text{m}$  holes was 0.318  $\mu\text{m}/(\text{nC}/\mu\text{m}^2)$ , and was extremely repeatable over the two weeks used to collect the data. For instance, in order to simulate a via of length 1.3  $\mu\text{m}$  in the 2.5  $\mu\text{m}$   $\text{SiO}_2$  layer, a 5  $\mu\text{m} \times 5 \mu\text{m}$  hole is first milled for  $(1.2 \mu\text{m}) / (0.318 \mu\text{m}/(\text{nC}/\mu\text{m}^2)) = 3.77 \text{ nC}/\mu\text{m}^2$ , and then a via is drilled through the remaining  $\text{SiO}_2$ .

A microprobe station functioning in two-point mode with a Keithley 2602 Sourcemeter was used to measure the resistances of the vias. The measured resistance includes contributions from the W pads, the W vias, and the Al layer. The contribution of the Al sheet to the total resistance was measured to be  $\sim 5 \Omega$  as determined by transmission line methodology and was subtracted from the data (Ref 6). The Keithly 2602 typically sourced from 10 to 100  $\mu\text{A}/\mu\text{m}^2$  through the via, yielding voltages on the order of 0.1 mV to 1 mV depending on the resistance. The resistance was the slope of the resulting  $I$ - $V$  curve.

The Vectra Vision FIB uses  $\text{W}(\text{CO})_6$  to make conductive W lines and vias. The usual deposition rate for W on a flat surface is  $0.17 \pm 0.01 \mu\text{m}/(\text{nC}/\mu\text{m}^2)$ , independent of beam current. For example, with a 23 pA beam, a pixel spacing of 0.03  $\mu\text{m}$ , and a dwell time of 0.5  $\mu\text{s}$ , the Vectra Vision system deposits a dose of 1  $\text{nC}/\mu\text{m}^2$  over an area  $1 \times 2 \mu\text{m}$  in 3.5 min to make a W layer 0.17  $\mu\text{m}$  thick. This rate for W deposited on a flat surface has never varied. The typically measured stoichiometry of the W metal is 65 at.% W, 8 at.% Ga, 5 at.% O, and 22 at.% C as determined with a Quantum 2000 Electron Spectroscopy for Chemical Analysis (ESCA) system (Ref 3, 5, 7). The resistivity of jumpers drawn on a  $\text{SiO}_2$  surface measured 250  $\mu\Omega \text{ cm}$ , in good agreement with the accepted value (Ref 3, 5). Pure W has a resistivity of 5.3  $\mu\Omega \text{ cm}$  (Ref 8).

Auger electron spectroscopy (AES) from a Phi 680 Scanning Auger Microscope was used for measuring compositional maps of the vias in cross section (Ref 7). The Phi 680 has SEM imaging capabilities with  $\sim 10 \text{ nm}$  spatial resolution and compositional accuracy of several atomic percentages. After making test vias along the edge of a piece of the test wafers, the  $\text{Ga}^+$  beam in the Vectra Vision is used to slice down the middle of the vias. A light sputter (2 nm) with a low sputter voltage (2 kV) to avoid preferential sputtering of C atoms over W atoms in the Phi 680 removed surface contamination from transport in air.

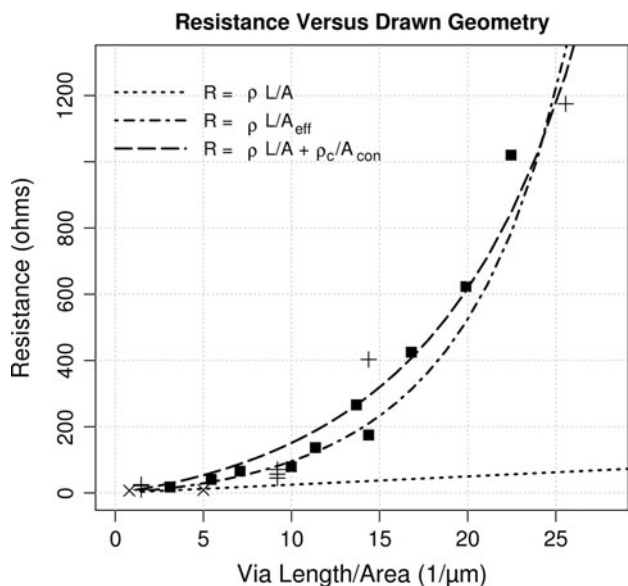


Fig. 1 Tungsten via resistance vs. aspect ratio

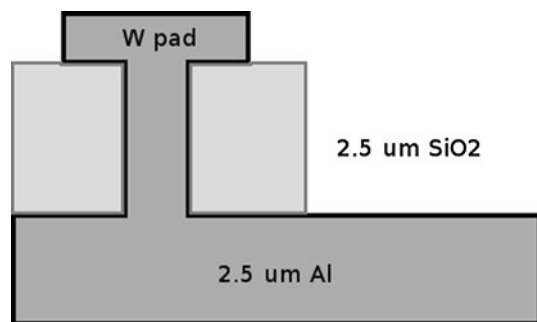


Fig. 2 Structural presentation of via measurement geometry

### 3. Results and Discussion

A general model for the resistances of the vias that uses a classical electromagnetic equation of the form  $R = \rho L/A$  and accounts for an effective area and a specific contact resistance at the W/Al interface reads as

$$R = \rho L/A_{\text{eff}} + R_c/A_{\text{con}}, \quad (\text{Eq } 2)$$

where  $A_{\text{eff}}$  is the effective area of the via and  $A_{\text{con}}$  is the contact area between the W and the Al.  $R_c$  is the specific contact resistance for the W/Al interface shown in Fig. 2 (Ref 6). One needs to be careful to understand the contact resistance since it has two distinct origins: (1) an intrinsic origin due to geometry and the specific contact resistance, and (2) an extrinsic

origin due to interface contamination. The extrinsic considerations include contamination from O and C in this case, premature end-pointing on the Al layer, or possibly the formation of a poorly conductive intermetallic layer from the Ga<sup>+</sup> beam, all which should serve to increase resistance. The intrinsic contribution includes current crowding and turning at the W/Al interface (Ref 4).

By varying L while the other parameters remain constant in Eq 2, one would expect a fit of the form  $y = mx + b$  with the slope determining  $\rho/A_{\text{eff}}$  and the intercept determining  $R_c/A_{\text{con}}$ . Figure 3 is a plot of the via's resistance as a function of its length L keeping the area constant at  $0.3 \mu\text{m} \times 0.3 \mu\text{m} = 0.09 \mu\text{m}^2$ . The specific contact resistance divided by the contact area is the y-intercept, which from the data is clearly insignificant to within experimental error. These data alone are strong evidence to label the contact resistance model for FIB vias as untenable.

Given the previous observations of  $\rho = 2.5 \Omega \mu\text{m}$  and a non-conductive skin  $\sim 0.1 \mu\text{m}$  thick, the expected slope from  $R = \rho L/A_{\text{eff}}$  would be  $\rho/A_{\text{eff}} = 250 \Omega/\mu\text{m}$  (Ref 3). Linear regression pegs the slope as  $220 \Omega/\mu\text{m}$ , in good agreement with the expectation for the effective area model.

Figure 4 shows Auger maps of the W, C, O, Al, Ga, and Si near the bottom of one of the vias. All signals except Ga are strong. The Ga signal was weak since it is a contaminant left by processing. The presence of Ga in the Al layer results from Ga implanted into the Al during the FIB cross section cut or during via fabrication.

An important observation from the maps of Fig. 4 is that the via penetrates  $\sim 0.2 \mu\text{m}$  into the Al layer, eliminating any possibility of a restricted contact area at the bottom of the via. The W/Al contact includes the bottom and some of the via sides, forcing the conclusion that  $A_{\text{con}} > A_{\text{eff}}$ . No evidence for excess C or O at the W/Al interface is extant, supporting the conclusion from Fig. 3 that invoking a finite value of the specific contact resistance  $R_c$  stemming from contamination at the W/Al interface is inappropriate. Furthermore, the Ga level does not appear appreciably different at the W/Al interface than elsewhere in the Al film, eliminating the possibility of W/Al/Ga

intermetallics. The lack of evidence to support an interface contact model leaves the effective area model as the remaining tenable model to explain the resistance data.

Developing a model to explain the presence of a poorly conductive lining along the walls of the via requires the definition two different forms of tungsten—primary W made from direct impact of the  $\text{W}(\text{CO})_6$  precursor with the 50 keV Ga<sup>+</sup> ion beam and secondary W made from impact of  $\text{W}(\text{CO})_6$  precursor with the scattered byproducts of the primary collision, including backscattered Ga<sup>+</sup> ions and derivatives from the cracked  $\text{W}(\text{CO})_6$  atoms. Figure 5 shows a drawing of the experimental setup used to demonstrate the existence of primary and secondary tungsten with ESCA.

The primary Ga<sup>+</sup> beam at 50 keV strikes the  $\text{W}(\text{CO})_6$  on the horizontal Si surface of Fig. 5, and scattered species will strike the  $\text{W}(\text{CO})_6$  on the vertical Si surface. The scattered species can

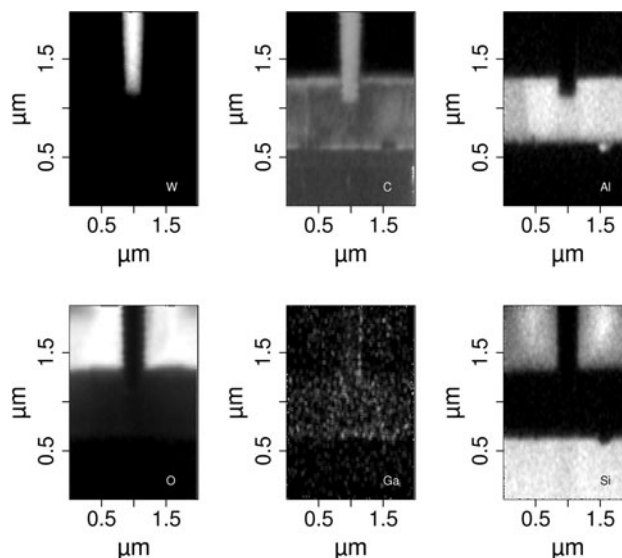


Fig. 4 Auger maps of the W, C, Al, O, Ga, and Si near the bottom of a  $0.3 \mu\text{m} \times 0.3 \mu\text{m}$  via

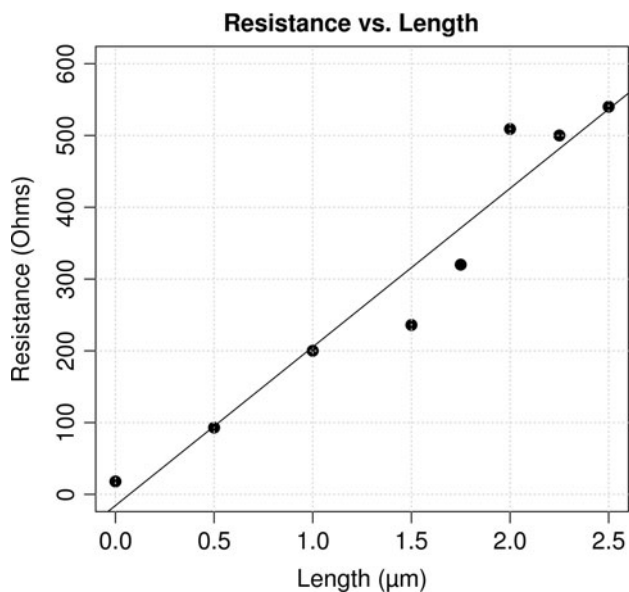


Fig. 3 Via resistance vs. length

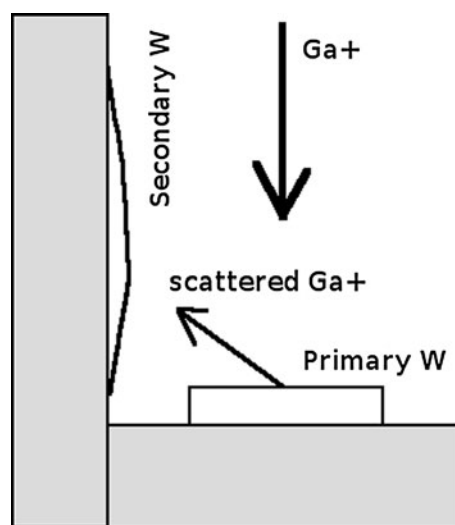


Fig. 5 Diagram of method to deposit and verify the existence of secondary W

have energies between 50 and 0 keV, with the majority having energies in the hundreds of eV range (Ref 7). The scattered  $\text{Ga}^+$  beam deposits  $W$  on the vertical surface. The secondary  $W$  contains partially reacted  $W(\text{CO})_6$  resulting from impact by low energy, scattered species.

A  $100\ \mu\text{m} \times 100\ \mu\text{m}$   $W$  pad was drawn on the horizontal surface, letting secondary  $W$  accumulate on the vertical surface. The chemical states of the  $W$ ,  $O$ , and  $C$  were measured with ESCA using a  $20\ \mu\text{m}$  x-ray beam. The appearance of a shiny  $W$  layer on the vertical surface was unmistakable to the naked eye, proving the existence of secondary  $W$ . Figure 6 shows the  $W\ 4f$  level for both the primary and secondary  $W$  films, along with a spectrum from a metallic  $W$  ingot for comparison. Both the primary and secondary  $W$  have measurable broadenings from the presence of  $C$  and  $O$  in the films. The secondary  $W$  is  $0.15\ \text{eV}$  broader than the primary  $W$ , indicative of more contamination in the film.

Figures 7 and 8 showing the  $O\ 1s$  and  $C\ 1s$  levels for primary and secondary  $W$  tell a more interesting story. The  $O\ 1s$  level shows the presence of two chemical valences—a rare occurrence since  $O$  is second only to  $F$  in electronegativity and usually has a valence of  $-2$ . Carbon monoxide has a small dipole moment with the positive end on the oxygen atom and a net charge of zero (Ref 9-11). The lack of negative charge in the oxygen valence shell allows the nuclear charge to pull the  $O\ 1s$  level to higher binding energy. The label  $(\text{CO})^0$  marks this form of  $\text{CO}$  at a binding energy  $E_B = 531.9\ \text{eV}$  in Fig. 7 with the interpretation that it is embedded carbon monoxide in the  $W$  thin-film.

The second peak in the  $O\ 1s$  level sits at  $E_B = 530.4\ \text{eV}$  and is consistent with  $\text{O}^{2-}$ . When attached to  $W$  in the form of  $W(\text{CO})_6$ , the carbon end of the carbonyl binds to the  $W$ , and the overall carbonyl takes a charge of  $-1$  electrons from the  $W$  atom (Ref 9, 10). The lower binding energy valence of oxygen corresponds to  $(\text{CO})^{-1}$  still bound to the  $W$ . The secondary  $W$  thin-film has relatively more  $(\text{CO})^{-1}$  than the primary  $W$  thin-film as a result of low energy bombardment from scattered species.

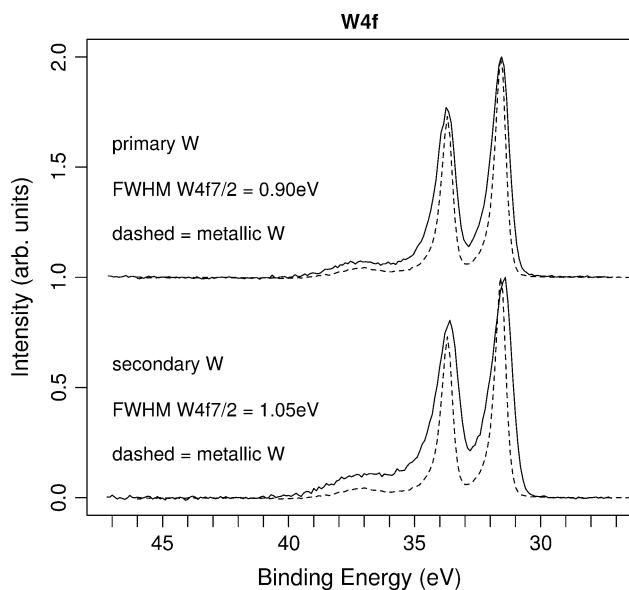


Fig. 6  $W\ 4f$  levels from primary and secondary tungsten

The  $C\ 1s$  level portrays a very similar story to the  $O\ 1s$  level, showing a higher binding energy peak at  $E_B = 284.5\ \text{eV}$  of  $(\text{CO})^0$  and a lower binding energy peak at  $E_B = 283.2\ \text{eV}$  of  $(\text{CO})^{-1}$ , and the secondary  $W$  once again shows more  $(\text{CO})^{-1}$  relative to the primary  $W$ .

The picture that emerges from the ESCA data is that the scattered species striking the vertical surface of Fig. 5 are not as efficient in converting the  $W(\text{CO})_6$  to metallic  $W$  as the higher energy  $\text{Ga}^+$  primary beam. The relevance of this observation is clear for a small area via formation. For the  $0.3\ \mu\text{m} \times 0.3\ \mu\text{m}$  via in Fig. 3, the via is created by milling through the  $\text{SiO}_2$  with a  $0.3\ \mu\text{m} \times 0.3\ \mu\text{m}$  raster, and then filled with a  $0.1\ \mu\text{m} \times 0.1\ \mu\text{m}$  raster (Ref 2). Typically, the raster is decreased by  $0.1\ \mu\text{m}$  per side to minimize deposition of  $W$  on the sidewalls

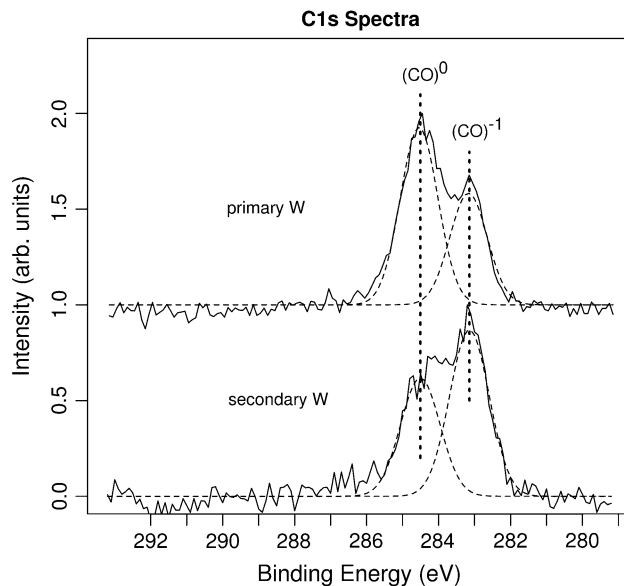


Fig. 7  $C\ 1s$  level from primary and secondary  $W$

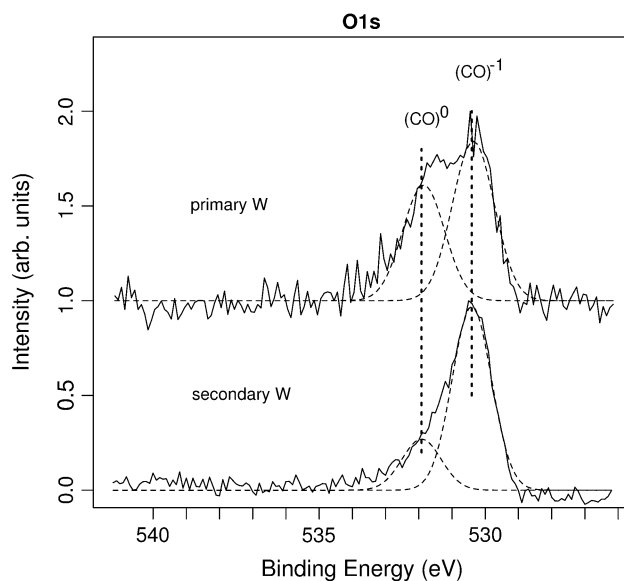


Fig. 8  $O\ 1s$  level in primary and secondary tungsten

near the top of the via that seals the opening and leaves a void in the middle of the via. The sidewalls must then be made of secondary W with a higher concentration of partially reacted, non-conductive  $W(CO)_6$ . One would expect a skin of non-conductive material on the side walls of about  $0.1 \mu\text{m}$  thick (Ref 3).

The use of the small spot ( $1 \text{ nm}$ ) of Auger to confirm this model by measuring secondary W on the via sidewalls themselves was unproductive because (1) Auger does not have the energy resolution required to discern the different chemical valences, and (2) the  $10 \text{ keV}$  energy of the Auger beam is sufficient to convert the remaining  $W(CO)_6$  in the sidewalls to something akin to primary W.

Allen et al. have created a closed-form analytical solution to the resistance of vias that correctly accounts for current crowding at the top and bottom of the via (Ref 4). The Allen model uses conservation of charge at both the top and bottom of the via to account for the added resistance due to current crowding and cornering at the ends of the via. The closed form analytical solution is a zeroth order Bessel function. Figure 9 shows the resistance data plotted against the width of the vias along with a Bessel function fit using Eq 11 of Ref 4 and the drawn geometry (dashed line). The drawn geometry does not account for a non-conductive perimeter. Parameters for the fit are:  $P_{c01} = P_{c02} = 0$ ,  $\rho = 2.5 \Omega \mu\text{m}$ ,  $R_{sh0} = 5.0 \Omega/\square$ , and  $R_{sh2} = 0.011 \Omega/\square$ . When plotted against the width, the data show a clear knee at a width of  $\sim 0.5 \mu\text{m}$  that marks a transition between low resistance, low aspect ratio vias, and high resistance, high aspect ratio vias. One can estimate that the transition between the two regimes occurs at a height to width ratio of  $\sim 5$ .

The dashed line underestimates the resistance at high aspect ratio as one would expect since it ignores the dead skin around the perimeter. The addition of a dead skin of width  $0.12 \mu\text{m}$  around the perimeter as shown for Fig. 1 improves the fit substantially (solid line). The width of  $0.12 \mu\text{m}$  was determined visually rather than by a proper least squares analysis. The fit still lacks some credibility at very small via widths and around widths of  $0.5 \mu\text{m}$ . Two factors could account for the lack of agreement: (1) the thickness of the non-conductive perimeter

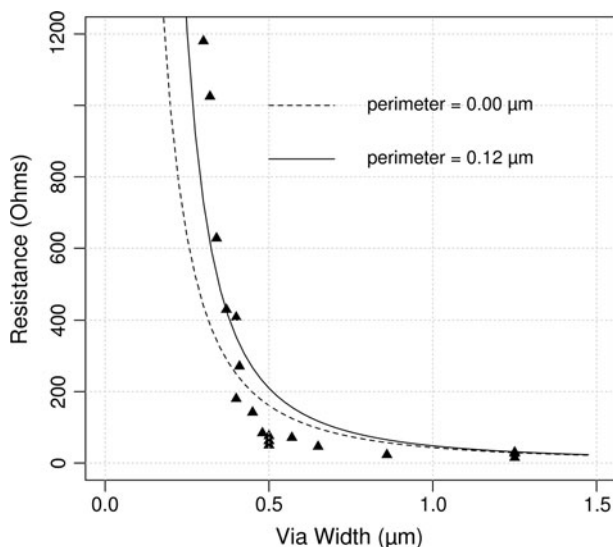


Fig. 9 Bessel function fit of resistance data

may not be constant but could, in principle, be a function of the via width, and (2) the Allen model assumes a circular via and not the square geometry used in these experiments. With regard to the first point, a primary conclusion of Ref 3 is that vias act like Faraday cups to trap reaction byproducts, and that vias of smaller widths trap byproducts more effectively than vias of larger widths. The assumption of a single perimeter thickness independent of via width is really fictitious rather than factual, and should be interpreted as a means for simplification.

With regard to the second point, the analytic solution presented in Ref 4 is based on a number of simplifications that may have resulted in the aforementioned test-analysis discrepancies. Chief among these simplifications is the presumption of axisymmetric geometry and boundary conditions. While the manufactured via is square and connected to opposed rectangular traces, the Allen model presumes a circular via with angularly symmetric potentials applied at the source and sink traces. In addition, these traces are infinite in radial extent and lack a thickness dimension. As a result, the calculated resistance from Ref 4 is predicated on axisymmetric current crowding, which departs from expectations with the experimental geometry.

In order to overcome the approximations of the analytic solution, a finite element model was developed. As depicted in Fig. 10, the model complies with the physical geometry, material allocation and boundary conditions. The resistivity,  $\rho$ , of the lower trace is  $0.03 \Omega \mu\text{m}$  and that of the via and upper trace is  $2.5 \Omega \mu\text{m}$ . As shown, a symmetry plane permits modeling half the structure. The dead skin is included by appropriately decreasing the outer dimension of the square via. The model solves Laplace's equation,  $\nabla^2 V = 0$ , with the boundary conditions  $V = 1$  applied at the end of one trace and  $V = 0$  at the end of the other. The figure details the mesh at the via-to-upper trace junction. Approximately 225000 hexahedral isoparametric 8 node elements are used in the model.

Figure 11 shows the current density distribution at the via-to-upper trace junction. The current density is decidedly not axisymmetric and, hence, divergent from the predictions of the analytic solution. Recognizing that a specified voltage drop is imposed on the structure, the applied current is calculated as the sum of  $-\rho \nabla V$  over the area of either trace end. Resistance is then easily derived from Ohm's law. Figure 12 presents typical finite element model-predicted resistances for various via dimensions. The predictions assume a dead skin depth of

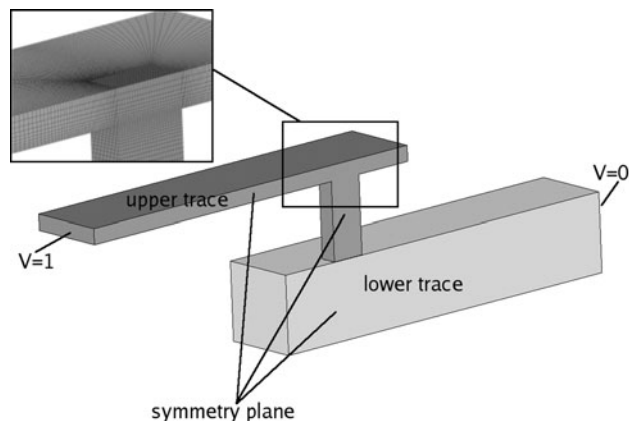
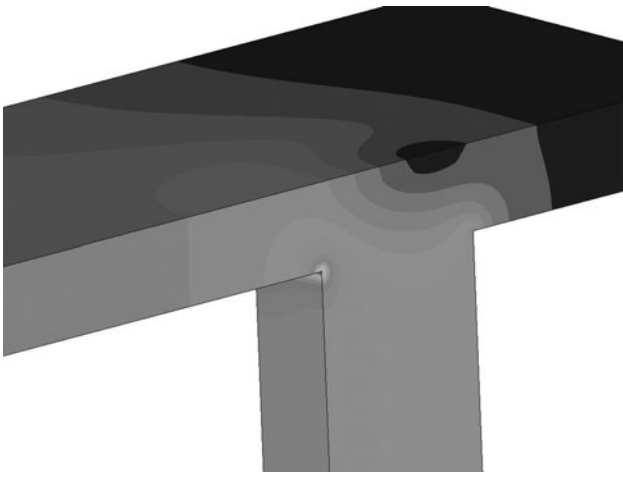
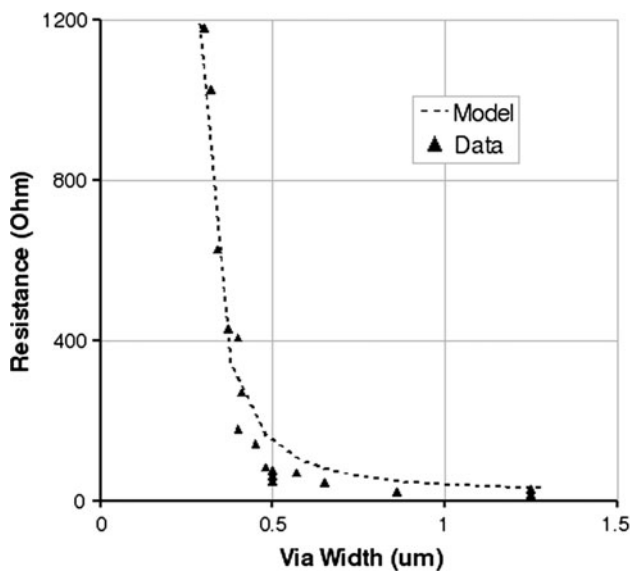


Fig. 10 A typical finite element model showing material composition and spatial discretization



**Fig. 11** Detail of the current density distribution at the via-to-upper trace interface (white is highest, black is lowest)



**Fig. 12** Finite element fit of resistance data

0.09  $\mu\text{m}$ , which is in agreement with the experimental findings. While the finite element predictions do not match the experimental data precisely, they do provide a better fit than the analytic solution, especially in the resistance knee that occurs for via widths between 0.45 and 0.8  $\mu\text{m}$  and at the smallest via widths measured.

## 4. Conclusions

High aspect ratio vias made with a FIB for the purpose of circuit editing work have a higher resistance than expected from classical electromagnetic theory and drawn geometries.

The elevated resistance is caused by a non-conductive skin around the perimeter that stems from the traditional technique for via filling while preventing pinch-off and void formation. FIB-made vias usually serve one of two purposes: either they tie a node to a supply voltage (ground or high), or they carry a signal. High resistance would probably not hamper the efficacy of vias of the first type, but vias of the latter type would likely be ineffective.

For second type of via, those carrying a signal, high resistance may have dire ramifications for flip-chip FIB strategies at technology nodes such as 65 nm, 40 nm, and beyond. The first encountered metal for flip-chip parts is metal 1 followed by metals 2, then 3, etc. The amount of available space to reach successively deeper metals becomes vanishing small as the technology node decreases. High-aspect ratio vias may often be the only way to reach deeper metal layers such as metal 3 and beyond. The circuit edit may be possible, but the resistance may prevent effective performance of the edited part. For such cases, closer collaboration between FIB engineers and circuit designers is critical to designing edits that alter functionality effectively and continue the viability of FIB to debug parts.

## Acknowledgment

The authors would like to thank David Leary of Avago Technologies for his support of the Failure Analysis Laboratory and to this study.

## References

1. J.R. Reitz, F.J. Milford, and R.W. Christy, *Foundations of Electromagnetic Theory*, 3rd ed., Addison-Wesley Publishing Company, Inc., 1980, p 140
2. V. Ray, N. Antoniou, N. Bassom, A. Krechmer, and A. Saxonis, Development of Void-free Focused Ion Beam-assisted Metal Deposition Process for Subhalf-micrometer High Aspect Ratio Vias, *J. Vac. Sci. Technol. B*, 2003, **21**(6), p 2715
3. D.W. Niles, J. Meyer, R.W. Kee, and M. DiBattista, An Analysis of Tungsten FIB-Fabricated Via Resistance, *Proceeding of the 34th International Symposium for Test and Failure Analysis*, Nov. 2-6, 2008 (Portland, OR), 2008, p 133
4. L.H. Allen, M.Y. Zhang, J.W. Mayer, E.G. Colgan, and R. Young, Solutions to Current Crowding in Circular Vias for Contact Resistance Measurements, *J. Appl. Phys.*, 1991, **70**(1), p 253
5. L. Gianuzzi and F. Stevie, *Introduction to Focused Ion Beams*, Springer, 2005
6. N. Stavitski, M.J.H. van Dal, A. Lauwers, C. Vrancken, A.Y. Kovalgin, and R.A.M. Wolters, Evaluation of Transmission Line Model Structures for Silicide-to-Silicon Specific Contact Resistance Extraction, *IEEE Trans. Electron. Devices*, 2008, **55**(5), p 1170
7. C.R. Brundle, C.A. Evans, Jr., and S. Wilson, *Encyclopedia of Materials Characterization*, Reed Publishing Inc., 1992
8. C. Kittel, *Introduction to Solid State Physics*, 5th ed., John Wiley and Sons, Inc., 1976, p 170
9. F.A. Cotton, G. Wilkinson, and P.L. Gaus, *Basic Inorganic Chemistry*, 3rd ed., John Wiley and Sons, Inc., 1995
10. F.A. Cotton and G. Wilkinson, *Advanced Inorganic Chemistry*, 5th ed., John Wiley and Sons, Inc., 1988
11. [http://www.webelements.com/compounds/tungsten/tungsten\\_hexacarbonyl.html](http://www.webelements.com/compounds/tungsten/tungsten_hexacarbonyl.html)